

**RESEARCH ARTICLE**

WILEY

# Assessing the blockage effect of wind turbines and wind farms using an analytical vortex model

Emmanuel Branlard<sup>1</sup>  | Alexander R. Meyer Forsting<sup>2</sup> 

<sup>1</sup>Wind Energy Department, National Renewable Energy Laboratory, Golden, Colorado, USA

<sup>2</sup>DTU Wind Energy, Technical University of Denmark, Roskilde, Denmark

## Correspondence to:

Emmanuel Branlard, National Renewable Energy Laboratory, 15013 Denver West Parkway, Golden, CO, USA.  
Email: emmanuel.branlard@nrel.gov

## Peer Review

The peer review history for this article is available at [publons.com/publon/10.1002/we.2546](https://publons.com/publon/10.1002/we.2546).

**Abstract**

Wind farm blockage effects are currently neglected in the prediction of wind farm energy yield, typically leading to an overestimation of the production. This work presents a novel method to assess wind farm production, while accounting for blockage effects. We apply a vortex model, based on a cylindrical wake, to assess induction effects. We present variations of the model to account for finite wake length, finite tip-speed ratios, and the proximity to the ground. The results are applied to single rotors in aligned and yawed conditions and to different wind farm layouts. We provide far-field approximations for faster estimates of the velocity field. Further, this article includes a new methodology to couple the induction model to engineering wake models, such as the ones present in the FLOW Redirection and Induction in Steady State (FLORIS). We compare the results to actuator disk simulations for various operating conditions of a single turbine and different wind farm layouts. We found that the mean relative error of the model in the induction zone is typically around 0.2% compared with actuator disk simulations. The computational time of the velocity field using the analytical vortex model is three orders of magnitude less than the one obtained with the actuator disk simulation.

**KEYWORDS**

actuator disk, induction zone, vortex models, wind farm blockage

## 1 | INTRODUCTION

The energy extraction from a wind turbine or wind farm induces a reduction of the upstream wind speed. This effect is referred to as “wind farm blockage,” and the area that is affected is called the induction zone. Wind farm developers and owners have turned their attention to this phenomenon because the current wind energy prediction procedures neglect wind farm blockage effects, resulting in an overprediction of the wind farm production (see, e.g., Meyer Forsting et al.<sup>1</sup>), and biases in power curve measurements. This work presents a novel methodology to assess wind farm production that accounts for wakes and blockage effects. The method is based on a reduced-order vortex model that is coupled to engineering wake models.

The upstream influence of a turbine is accounted for in the momentum theory presented by Rankine,<sup>2</sup> but quantitative analytical treatments are only made possible using vortex models such as the ones developed by Joukowski.<sup>3</sup> The vortex cylinder model was shown to provide results similar to momentum theory<sup>4,5</sup> and has been used to compute the entire velocity field about a wind turbine.<sup>6</sup> The model was later extended to

\*CFD, computational fluid dynamics, RANS, Reynolds-averaged Navier–Stokes, WIZ, wake and induction zone (software)

This is an open access article under the terms of the Creative Commons Attribution License, which permits use, distribution and reproduction in any medium, provided the original work is properly cited.

© 2020 The Authors. Wind Energy published by John Wiley & Sons Ltd

yawed conditions.<sup>7</sup> The formulae of the vortex cylinder model were, for instance, applied by Medici et al. to assess the velocity deficit on the axis upstream of a turbine<sup>8</sup> and applied to study different aspects of aerodynamics, such as dynamics inflow models,<sup>9,10</sup> far-wake models,<sup>11–13</sup> kite aerodynamics,<sup>14</sup> actuator surface methods,<sup>15</sup> or regularized actuator disks.<sup>16</sup>

The first engineering model to account for induction effects in wind farms was presented by the current authors using a vortex-based model.<sup>17</sup> Many additional investigations of the blockage effect using means other than vortex theory are found in the literature. Variations of power production in the front row of a wind farm has been observed from SCADA data.<sup>18</sup> Measurements using lidar technologies on full-scale wind farms can be found in the work of Asimakopoulos et al.<sup>19</sup> or Simley et al.<sup>20</sup> Field and wind tunnel measurements were also used by Howard and Guala and compared with previous models.<sup>21</sup> Computational fluid dynamics (CFD) methods, such as Reynolds-averaged Navier–Stokes (RANS) simulations, have also been used to assess the wind farm blockage effect.<sup>1,22,23</sup> Meyer Forsting et al.<sup>24</sup> include a comparison of the induction zone velocity with lidar measurements. A reduced-order model of the induction zone was derived assuming self-similarity of the flow and compared with CFD results.<sup>25</sup> CFD methods were also applied to the investigation of the induction zone in sheared inflows.<sup>26</sup> Attempts to take advantage of the blockage effect and the potential compression zones between narrowly spaced turbines were demonstrated by McTavish et al.<sup>27</sup>

This article uses a low-computational-cost model to assess the induction zone in front of wind turbines within a wind farm. The model is combined with wake models to compute the full velocity field in a wind farm. With this model, the prediction of wind farm power production accounts for the blockage effect. This work extends on the induction model previously presented by the authors.<sup>17</sup> In Section 2, we present the vortex model used to determine the velocity field in the induction zone of a wind turbine. We also describe the methodology to combine the induction model with wake models to obtain wind farm velocity fields and energy yields. In Section 3, we compare the single-rotor model with actuator disk simulations for an aligned or yawed wind turbine, and we present the influence of the ground effect on the induction zone. In Section 4, we apply the method to evaluate the velocity field and power production of wind farms of different layouts and hub heights. Limitations and possible extensions of the model are discussed in Section 5. The data and source code used for the analyses are publicly available in a Python software package called wake and induction zone (WIZ).<sup>28</sup>

## 2 | MODEL OF WIND TURBINE INDUCTION AND WIND FARM BLOCKAGE EFFECT

In this section, we present a method to assess wind turbine induction and wind farm blockage effects. Sections 2.1 to 2.3 describe the vortex model used to compute the induction for a single turbine. Section 2.4 presents the methodology to combine this model with wake models to obtain realistic velocity fields within wind farms and assess their power production.

### 2.1 | Introduction to the vortex model

The coordinate system and the vortex model are presented in Figure 1A–C. The  $x$ -axis is normal to the rotor, pointing downstream, the  $z$ -axis is pointing vertically, and the origin of the system is located at the rotor center. The radial coordinate,  $r$ , is introduced, such that  $r^2 = y^2 + z^2$ . The free-stream velocity norm is written as  $U_0$  and assumed to be uniform. The effects of shear and turbulence are not considered but will be discussed in Section 5. For aligned flow, the free-stream velocity is along  $x$ ,  $\mathbf{U}_0 = U_0 \mathbf{e}_x$ , whereas for yawed inflow, it is  $\mathbf{U}_0 = U_0 \cos \theta_{\text{yaw}} \mathbf{e}_x + U_0 \sin \theta_{\text{yaw}} \mathbf{e}_y$ , with  $\theta_{\text{yaw}}$  the yaw angle, positive around  $z$ . The vortex cylinder model is inspired by the cylindrical model of Joukowski.<sup>3</sup> It represents an actuator disk and its wake by assuming a prescribed support of vorticity. For simplicity, expansion of the vorticity surface is neglected.<sup>†</sup> The rotor and its wake are assumed to be contained within a cylinder of radius,  $R$ , equal to the rotor radius. In yawed flows, the wake axis,  $\xi$ , forms an angle,  $\chi$ , referred to as the “skew” angle, with the direction normal to the disk. In this study, we use the empirical relationship given by Burton et al.<sup>29</sup> to obtain the skew angle, as a function of the mean axial induction,  $\bar{a}$ , or the thrust coefficient,  $C_T$ :

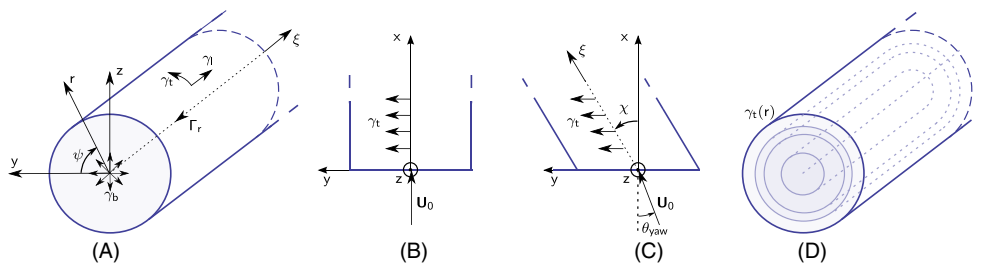


**FIGURE 1** The vortex cylinder model. A, Three-dimensional representation of the model, showing the different components of vorticity:  $\gamma_t$ ,  $\gamma_l$ ,  $\gamma_b$  and  $\Gamma_r$ . The study focuses on  $\gamma_t$ . B, Top view for aligned flow. C, Top view for yawed flow: definition of the yaw angle,  $\theta_{\text{yaw}}$ , and skew angle,  $\chi$ . D, Concentric superposition of cylinder models [Colour figure can be viewed at [wileyonlinelibrary.com](http://wileyonlinelibrary.com)]

$$\chi = \theta_{\text{yaw}}[1 + 0.6 \bar{a}] = \theta_{\text{yaw}} \left[ 1 + 0.3 \left( 1 - \sqrt{1 - C_T} \right) \right]. \quad (1)$$

The model is referred to as “elementary” when the rotor circulation is uniform. In this case, a single vortex cylinder is used to model the wake. The model for a radial variation of circulation is obtained by the superposition of elementary models, as illustrated in Figure 1D and further detailed in Appendix A1. No variation of the circulation with the azimuth will be considered.<sup>‡</sup> The elementary model consists of the following vorticity components<sup>6,30</sup>: a straight vortex line at the root, a cylinder supporting tangential and longitudinal vorticity, respectively, noted  $\gamma_t$  and  $\gamma_l$ , and a disk of bound vorticity extending radially, noted  $\gamma_b$ . The tangential vorticity surface formed by  $\gamma_t$  can be thought of as a continuous distribution of vortex rings, parallel to the rotor plane. The combination of the root vortex, bound vorticity, and longitudinal vorticity forms a closed system that introduces swirl in the wake. In most of this article, we assume the cylindrical surface to be semi-infinite. The extension of the model to a finite length cylinder is presented in Appendix C1. The induced velocities from the vortex system are obtained using the Biot–Savart law and will be noted with the lowercase variable  $\mathbf{u}$ . They are summed with the free-stream velocity to obtain the total velocity field:

$$U_x = U_0 \cos \theta_{\text{yaw}} + u_x, \quad U_y = U_0 \sin \theta_{\text{yaw}} + u_y, \quad U_z = u_z \quad (\text{and for axisymmetric flows: } U_r = u_r). \quad (2)$$

The current study focuses on the axial velocity,  $U_x$ , and the tangential vorticity component,  $\gamma_t$ ,<sup>§</sup> but all components may be computed from this model and are included in the numerical package WIZ.<sup>28</sup>

For the elementary models presented in Section 2.2, the tangential vorticity may be determined as

$$\gamma_t = -U_0 \left[ 1 - \sqrt{1 - C_T} \right] = -2U_0 \bar{a}, \quad (3)$$

where  $C_T$  is the total thrust coefficient of the rotor. In this specific case,  $\gamma_t$  is directly related to the mean axial induction at the rotor,  $\bar{a}$ . Alternative formulae to Equation 3 are provided in Section 3.6 based on calibrations against actuator disk simulations. Finer details, such as for flows near the rotor, may be obtained by using the method presented in Appendix A1. The following paragraphs present the induced velocity formulae from the vorticity model, which will be used to determine the velocity upstream of wind turbines in Sections 3 and 4.

## 2.2 | Velocity field obtained with the elementary vortex model

In its general form, the velocity induced by the elementary vortex model is written as  $\mathbf{u}_{\text{elem}}(\mathbf{x}, R, \gamma_t)$ , where  $\mathbf{x}$  is the point of evaluation,  $R$  is the cylinder radius, and  $\gamma_t$  is the vortex cylinder intensity. The subscript and dependency in  $R$  and  $\gamma_t$  will be omitted in this section for conciseness and reintroduced in the following sections. We will write  $\mathbf{u}_{\text{elem}}(x, r) = \{u_x, u_r\}$  for axisymmetric flows, and  $\mathbf{u}_{\text{elem}}(x, y, z) = \{u_x, u_y, u_z\}$  otherwise. The formulae presented in this section are for a semi-infinite cylinder. The extension of the model to a finite length cylinder is presented in Appendix C1. Further, the far-field formulae presented in Appendix B1 may be used to speed up the computation of the velocity field.

### 2.2.1 | Aligned flow

The velocity induced by the vortex cylinder model in aligned flow is obtained by integrating the Biot–Savart law as<sup>6</sup>

$$u_x(x, r) = \frac{\gamma_t}{2} \left[ \frac{R-r+|R-r|}{2|R-r|} + \frac{xk(x, r)}{2\pi\sqrt{rR}} \left( K(k^2(x, r)) + \frac{R-r}{R+r} \Pi(k^2(0, r), k^2(x, r)) \right) \right], \quad k^2(x, r) = \frac{4rR}{(R+r)^2 + x^2} \quad (4)$$

$$u_r(x, r) = -\frac{\gamma_t}{2\pi} \sqrt{\frac{R}{r}} \left[ \frac{2-k^2(x, r)}{k(x, r)} K(k^2(x, r)) - \frac{2}{k(x, r)} E(k^2(x, r)) \right], \quad (5)$$

where  $K$  and  $\Pi$  are the complete elliptic integrals of the second and third kind and where  $k$  is the elliptic parameter. Equation 4 takes a simple form on the  $x$ -axis:

<sup>‡</sup>This choice appears satisfactory, even for yawed inflow, because most yaw models of blade element momentum codes (Coleman or Glauert model) rely on this assumption.<sup>31,32</sup>

<sup>§</sup>In aligned flows, only  $\gamma_t$  contributes to  $u_x$  and  $u_r$ . In yawed flows,  $\gamma_l$  will also contribute to these velocities. Yet the contributions are of second order<sup>7</sup> and can be neglected when considering inductions within a wind farm.

$$u_x(x, r=0) = \frac{\gamma_t}{2} \left[ 1 + \frac{x}{\sqrt{R^2 + x^2}} \right], \quad \text{and in the far-field: } u_x(x, r=0) \underset{x \rightarrow -\infty}{\sim} \frac{\gamma_t R^2}{4x^2} \left[ 1 - \frac{R^2}{x^2} + o\left(\frac{R^4}{x^4}\right) \right]. \quad (6)$$

The Taylor expansion given on the right side of Equation 6 will be compared with the doublet approximation in Appendix B1. Using Equation 6, the total axial velocity,  $U_x = U_0 + u_x$ , takes a simple form along this axis:

$$U_x(x, r=0) = U_0 + u_x(x, r=0) = U_0 \left[ 1 - \bar{a} \left( \frac{x}{\sqrt{R^2 + x^2}} \right) \right], \quad (7)$$

where the axial induction factor, as defined by Equation 3, was introduced. Equation 7 is a convenient formula for evaluating the velocity upstream of a turbine or assessing near-wake expansion using mass conservation.<sup>33</sup>

## 2.2.2 | Yawed flow

The elementary vortex model in yawed flow is illustrated in Figure 1C. The velocity field induced by this model is given as<sup>7</sup>

$$u_{\bullet}(x, r, \psi) = \frac{\gamma_t}{4\pi} \int_0^{2\pi} \frac{a'_{\bullet} c + b'_{\bullet} a}{a(ac-b)} d\theta', \quad (8)$$

where the symbol  $\bullet$  stands for  $x$ ,  $y$ , or  $z$  and the different coefficients are

$$a'_x = R[R - r \cos(\theta' - \psi)], \quad b'_x = mR \cos \theta', \quad a'_y = Rx \cos \theta', \quad b'_y = -R \cos \theta', \quad a'_z = Rx \sin \theta', \quad b'_z = -R \sin \theta', \quad (9)$$

$$a^2 = R^2 + r^2 + x^2 - 2rR \cos(\theta' - \psi), \quad b = m(r \cos \psi - R \cos \theta') + x, \quad c^2 = 1 + m^2, \quad m = \tan \chi \quad (10)$$

with  $\psi$  the azimuthal angle, such that  $y = r \cos \psi$  and  $z = r \sin \psi$ , as illustrated in Figure 1A.

## 2.3 | Modeling the ground effect

The proximity of the ground has an impact on the flow field and turbine performance. The main effect is captured by the model by considering a no-flow-through or “slip” condition at the ground. When this effect is discarded, the vorticity generated by the turbine will induce a flow through the ground, which would be unphysical. To compensate for this flow, a distribution of sources could be placed on the ground, and their induced velocity would counteract this flow. Equivalently, a “mirror” vorticity distribution may be placed symmetrically with respect to the ground. This approach is illustrated in Figure 2. The velocity field is obtained by summing the velocity fields induced from two elementary models, mirrored with respect to the ground. Assuming the ground is located as  $z = 0$  and the wind turbine hub center is located at  $\mathbf{x}_h = (x_h, y_h, z_h)$ , the velocity field is

$$\mathbf{U}(x, y, z) = \mathbf{U}_0 + \mathbf{u}_{\text{elem}}(x - x_h, y - y_h, z - z_h) + \mathbf{u}_{\text{elem}}(x - x_h, y - y_h, z + z_h). \quad (11)$$

The method is similarly applied to the superposition of cylinders presented in Appendix A1.

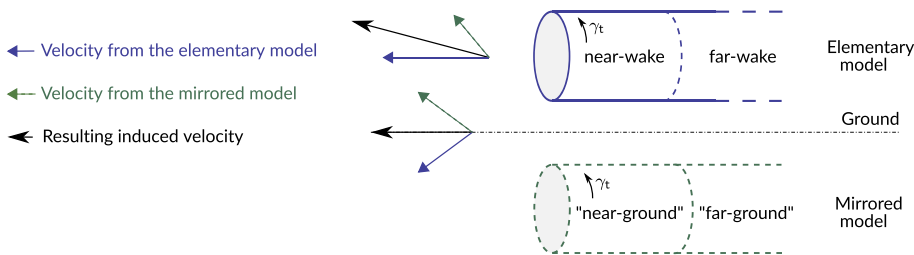
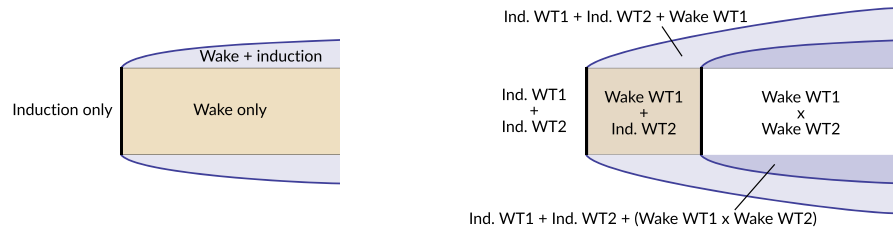


**FIGURE 2** Illustration of the mirrored vortex model used to account for the ground effect. The vorticity distribution has the same orientation on both sides of the ground. The resulting induction is greater in front of the rotor and satisfies the slip condition at the ground [Colour figure can be viewed at [wileyonlinelibrary.com](http://wileyonlinelibrary.com)]

**FIGURE 3** Coupling of the vortex cylinder induction model with the wake model. Left: one turbine. Right: two turbines (WT1 and WT2). The “+” sign indicates that velocity fields are added, whereas “x” indicates a flow field merging [Colour figure can be viewed at [wileyonlinelibrary.com](http://wileyonlinelibrary.com)]



## 2.4 | Coupling of the induction model with wake models for wind farm flow modeling

In this section, we present a method to compute the velocity field and power production of a wind farm, while accounting for blockage effects. The method only uses the velocity field from the vortex model to account for upstream “induction” effects, and not for downstream wake effects. Indeed, the velocity field obtained from the vortex cylinder model is not representative behind the rotor because wake diffusion and expansion are neglected by this model. To alleviate this issue, we use engineering wake models to represent the wake velocity field and the vortex model to represent the induction zone velocity field. Typical wake models, such as the ones integrated in the FLOW Reduction and Induction in Steady State (FLORIS) model, are the N.O. Jensen model, the Gauss model, or the curl-wake model.<sup>34</sup>

The methodology used to couple the vortex cylinder induction model with a wake model is illustrated in Figure 3. For the coupling, the velocity induced by the vortex cylinder model is enforced to be zero inside the cylinder volume and on the rotor plane, that is, inside the domain delimited by  $x \leq 0$  and  $r \leq R$ .<sup>¶</sup> The reason for setting the velocity to zero inside the cylinder volume is that wake models are assumed to be more accurate in this region. In Figure 3, this region is indicated by the label “wake only”, since only the velocity field from the wake model is used there. The reason for setting the vortex cylinder induction to be zero on the rotor plane is that, in the FLORIS framework, the average velocity on the rotor disk is used to assess the “free-stream” velocity. This velocity should not contain the self-induced velocity from the current turbine but should include the influences from all wakes and the inductions from all other turbines. The velocity is set to zero on grid points surrounding the rotor plane to make sure this condition is satisfied. Outside of this volume, the velocity field from the “induction” and wake models are superimposed. This forms the baseline flow field about a turbine illustrated on the left of Figure 3.

When multiple turbines are present, the wake velocities are merged according to the methods implemented in FLORIS, whereas the “induction” velocities are superposed to the field afterward. Wake merging methods have been used successfully by the community. The induction field is assumed to be a weak perturbation, which justifies the linear superposition,

The induction affects the loading of the upstream turbine, whereas the wake affects the loading of the downstream turbine. For this reason, several iterations are run to ensure that the wind farm flow field and the turbines’ loading are consistent. The algorithm is as follows. The mean undisturbed wind field in the wind farm is constant and noted  $\mathbf{U}_0$ . The induction field is initialized to zero,  $\mathbf{u}_{\text{ind}} = 0$ . The following steps are performed for each iteration of the algorithm:

- Compute the base flow field as  $\mathbf{U}_{\text{base}} = \mathbf{U}_0 + \mathbf{u}_{\text{ind}}$
- Perform a wake computation procedure in the entire wind farm (typically from upstream to downstream). The number of turbines is noted  $n$ , and the turbines are labeled using  $i = 1 \dots n$ . The “free-stream” velocity of each turbine is computed from the sum of the base field,  $\mathbf{U}_{\text{base}}$ , and upstream wake fields. By design of  $\mathbf{u}_{\text{ind}}$ , this free-stream velocity does not contain the induction from the current turbine but contains the induction from all other turbines. The free-stream velocity of each turbine is used to assess its thrust coefficient,  $C_{T,i}$ , and hence generate a wake flow field downstream of the current turbine. The total wake flow field,  $\mathbf{u}_{\text{wake}}$ , is determined by merging the different wake fields together.
- Compute the induction field in the entire wind farm. The thrust coefficients determined in the previous step are used to compute  $\gamma_{t,i}$  for each turbine, using Equation 3 (or Equation 15). The velocity field from the vortex cylinder models of each turbine are superposed to each other, after ensuring that each field is 0 on the rotor and in the cylindrical wake zone. The variable  $\mathbf{u}_{\text{ind}}$  is updated as

$$\mathbf{u}_{\text{ind}} = \sum_{i=1}^n \left[ \mathbf{u}_{\text{elem}}(x - x_{h,i}, y - y_{h,i}, z - z_{h,i}, \gamma_{t,i}) + \mathbf{u}_{\text{elem}}(x - x_{h,i}, y - y_{h,i}, z + z_{h,i}, \gamma_{t,i}) \right] \delta_{\text{ind-zone},i}, \quad (12)$$

where  $x_{h,i}$  is the position of the hub center of turbine  $i$  and  $\delta_{\text{ind-zone},i}$  is a function that is equal to 1 in the induction zone of turbine  $i$ , and 0 otherwise.

- Exit the iteration loop if the park performance (power of each turbine) has converged from the previous iteration to the current one.

<sup>¶</sup>Alternatively, the flow can be set to zero in the half-domain behind the rotor ( $x \leq 0$ ) and not just in the cylinder volume ( $(x \leq 0) \cup (r \leq R)$ ).

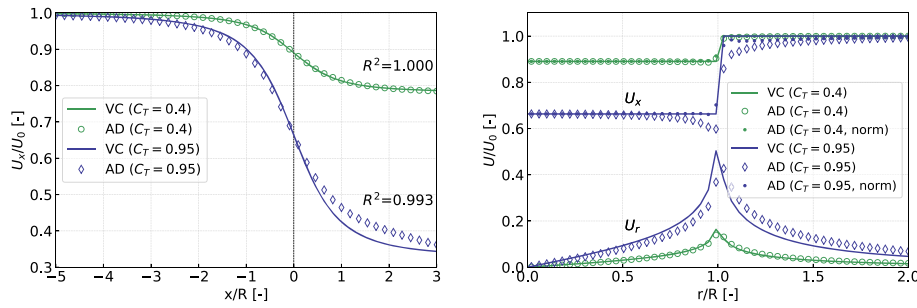


**FIGURE 4** Velocities obtained by the vortex cylinder (VC) model and actuator disk (AD) simulation for the two thrust coefficients,  $C_T$ . (Left) Axial velocity along the rotor axis; (right) axial and radial velocity along the rotor radius [Colour figure can be viewed at [wileyonlinelibrary.com](http://wileyonlinelibrary.com)]

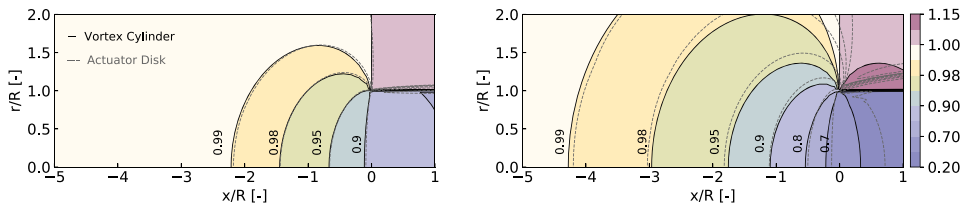


**FIGURE 5** Axial velocity contours normalized by the free-stream velocity ( $U_x/U_0$ ), as obtained by the vortex cylinder model (—) and actuator disk simulations (---) for  $C_T = 0.4$  (left) and  $C_T = 0.95$  (right) [Colour figure can be viewed at [wileyonlinelibrary.com](http://wileyonlinelibrary.com)]

At the end of the iterations, the full velocity field is computed as  $\mathbf{U} = \mathbf{U}_0 + \mathbf{u}_{\text{ind}} + \mathbf{u}_{\text{wake}}$ . Results from this methodology are presented in Section 4, while approximations and limitations are discussed in Section 5.

### 3 | INDUCTION ZONE IN FRONT OF A WIND TURBINE

The model presented in Section 2 is compared against actuator disk simulations in this section to assess its ability to accurately evaluate the induction zone in front of a single turbine. The model will be further applied to wind farms in Section 4. The 3D flow solver EllipSys3D developed at the Technical University of Denmark was used to perform RANS actuator disk simulations.<sup>35,36</sup> The actuator disk formulation discretizes the disk by a polar grid and distributes the forces in the flow domain according to the intersectional grid between the disk and flow mesh. The method avoids pressure–velocity decoupling via a Rhie–Chow-like approach.<sup>37,38</sup> The numerical setup of these simulations is described in Troldborg and Meyer Forsting.<sup>25</sup> The fact that actuator disk simulations are taken as reference is discussed in Section 5.

The vorticity and momentum formulations of an actuator disk are two equivalent formulations. The vortex model presented in Section 2 is an approximation of the vortex actuator disk that does not account for wake expansion. This will be the fundamental source of discrepancies between the models. Yet it will be shown that the vortex cylinder model provides results with great accuracy, for a computational time three orders of magnitude less than the actuator disk simulations.

#### 3.1 | Aligned rotor without swirl

In this section, we simulate a nonrotating actuator disk with a uniform thrust coefficient,  $C_T$ . The axial velocities from both models along the rotor axis are shown on the left of Figure 4 for  $C_T = 0.4$  and  $C_T = 0.95$ , corresponding to  $\gamma_t = -0.23U_0$  and  $\gamma_t = -0.78U_0$ , respectively. The choice of  $C_T$  value covers the typical range of operating conditions of a wind turbine.<sup>#</sup> The axial velocity is directly obtained from Equation 7 for the vortex cylinder model. Radial velocities along the rotor radius are also given on the right of Figure 4. The coefficients of determination,  $R^2$ , between the curves are shown in the figure. A strong agreement between the actuator disk and vortex cylinder results is found for the low-thrust coefficients. The wake expansion is limited for such operating conditions, and we expect the wake shape to be well approximated by a cylinder. This approximation deteriorates as the thrust coefficient increases, which explains the differences observed for  $C_T = 0.95$ . As described by van Kuik and Lignarolo,<sup>11</sup> the axial induction is not uniform along the rotor span, yet the norm of the velocity is approximately constant (see the curve labeled “AD (norm)” on the right of Figure 4). The velocity fields from both models are compared in Figure 5 for  $C_T = 0.4$  and  $C_T = 0.95$ . A quantitative assessment of the difference between the models in the induction zone is provided in Section 3.3 for the more challenging case of yawed inflow, providing a conservative estimate of the error in the aligned case.

<sup>#</sup>The value  $C_T = 0.95$  is a challenging case, above which the wake starts becoming turbulent and the vortex model and RANS assumptions may no longer be realistic.<sup>39</sup> High  $C_T$  values are only reached around the cut-in region of the wind turbine or when the turbine is operating in off-design conditions, which is more likely to happen for tightly spaced layouts with strong wakes impacting the turbines intermittently.

### 3.2 | Aligned rotor with swirl

We simulate a rotating actuator disk for different thrust coefficients and tip-speed ratios. The thrust coefficient is set to increase linearly from zero and reaches a constant value at the spanwise position,  $r = 0.1R$ . This follows the approach of Madsen et al.<sup>40</sup> and avoids unphysical singularity at the root of the rotor. The spanwise circulation strength in the vortex cylinder model is obtained by solving Equation A1 using the thrust coefficient distribution from the actuator disk simulation. The velocity contours from both models are visually compared on the left of Figure 6 for a thrust coefficient of 0.4 and a tip-speed ratio of 2. Both models agree on the prediction of the blockage effect. The impact of the swirl is clearly visible at the root of the rotor, but its impact upstream is limited. The error between the two models is further evaluated for different thrust coefficients,  $C_T \in \{0.4, 0.95\}$ , and tip-speed ratios,  $\lambda \in \{2, 6, 10, \infty\}$ , in a rectangular area delimited by  $x = [-3R, 0.1R]$  and  $|r| < 0.9R$ . The errors (not shown) are maximal near the rotor rim, where the effect of near-wake expansion is the strongest but also where the singularity of the vortex model and the inherent smearing of the numerical model are expected to be in disagreement. The error between the models are reported on the right of Figure 6. The mean relative error of the velocity reaches 0.4% for the case  $\lambda = \infty$  and  $C_T = 0.95$ , whereas lower relative errors are obtained for the other operating conditions considered.

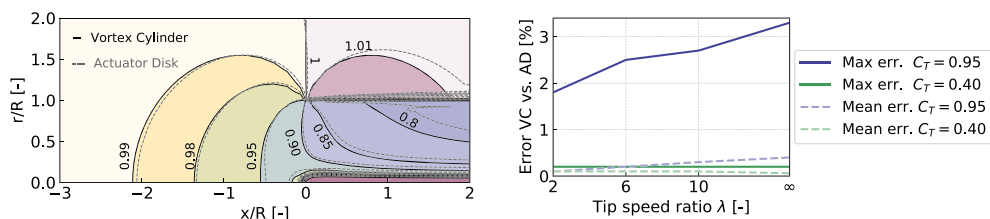
### 3.3 | Rotor in yaw

In this section, we consider a nonrotating actuator disk, yawed by an angle of  $\theta_{yaw} = 30^\circ$ . A uniform thrust coefficient is prescribed for both models. Similar results than the one presented in Figure 4 are now given in Figure 7 for  $\theta_{yaw} = 30^\circ$ . The observation from this figure follows the same conclusions drawn regarding Figure 4, though the coefficient of determinations are lower in this yawed case. It is worth noting that the axial velocity along the skewed wake axis (labeled "VC") is well approximated by evaluating Equation 7 with  $x = \xi$  (curve labeled "VC (straight)").

Contours of the axial velocity for the cases considered are shown in Figure 8. At  $C_T = 0.4$ , the blockage effect predicted by both tools is in fair agreement. Differences in the velocity contours are yet observed for the case  $C_T = 0.95$ , which can be attributed to the differences in wake expansion visible in the figure. These differences are further quantified. The mean and maximum relative error between the two models is calculated within a zone delimited by  $x \in [-3R, 0.1R]$  and  $|r| < 0.9R$ . The vicinity of the disk is purposely avoided because strong effects are expected at the rim of the disk. The mean and maximum relative error for  $C_T = 0.4$  are 0.1% and 0.8%, respectively. These values are 1.3% and 7.4%, respectively, for  $C_T = 0.95$ .

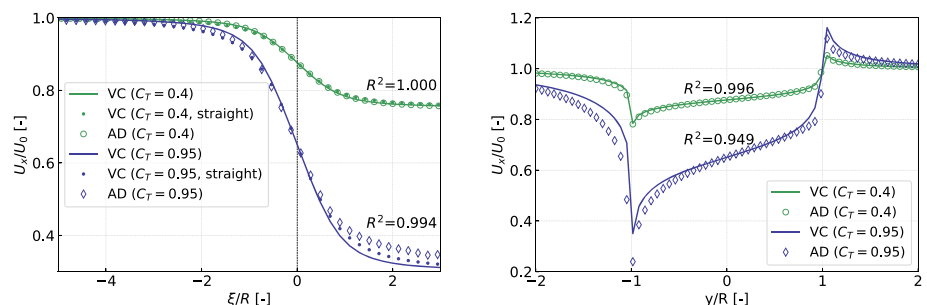
### 3.4 | Ground effect

We introduce the ground effect using a mirrored vorticity, as described in Section 2.3. In the actuator disk simulations, we apply the equivalent "slip" condition at the ground boundary. The axial velocity fields in a vertical plane obtained from both methods are shown in Figure 9 for a hub height of  $1.5R$  and for two thrust coefficients. The agreement between the vortex cylinder and actuator disk results is again observed to be strong



**FIGURE 6** Aligned rotor with swirl. (Left) Axial velocity contours for  $C_T = 0.4$  and  $\lambda = 2$ . Black and gray contours are used for the vortex cylinder model and actuator disk simulations; (right) mean and maximum relative errors between the axial velocities obtained by the models in the induction zone [Colour figure can be viewed at [wileyonlinelibrary.com](https://onlinelibrary.com)]

**FIGURE 7** Velocities obtained by the vortex cylinder (VC) and actuator disk (AD) models for two thrust coefficients:  $C_T$  and  $\theta_{yaw} = 30^\circ$ . (Left) Axial velocity along the skewed wake axis; (right) axial and radial velocity along the rotor radius [Colour figure can be viewed at [wileyonlinelibrary.com](https://onlinelibrary.com)]



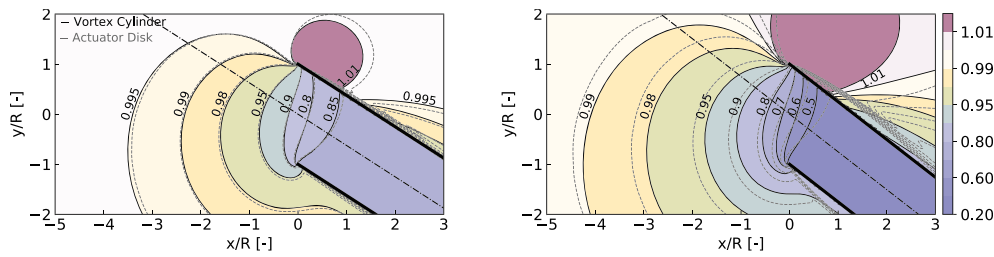


**FIGURE 8** Velocities obtained by the vortex cylinder model and actuator disk simulation for a rotor yawed by  $30^\circ$ , with  $C_T = 0.40$  (left) and  $C_T = 0.95$  (right) [Colour figure can be viewed at [wileyonlinelibrary.com](http://wileyonlinelibrary.com)]

**TABLE 1** Relative error in axial velocity between the actuator disk (AD) simulation and vortex cylinder (VC) model for different thrust coefficients ( $C_T$ ), hub heights ( $H$ ), and upstream locations ( $x$ )

	$C_T = 0.4$			$C_T = 0.7$			$C_T = 0.95$		
	$H = 1.5R$	$H = 2R$	$H = \infty$	$H = 1.5R$	$H = 2R$	$H = \infty$	$H = 1.5R$	$H = 2R$	$H = \infty$
AD velocity at $x = -2R$ ( $\%U_0$ )	98.52	98.65	98.83	96.86	97.12	97.49	94.52	94.96	95.71
Rel. error, VC w.r.t. AD (%)	0.07	0.06	0.01	0.40	0.36	-0.01	1.22	1.12	0.77
AD velocity at $x = -5R$ ( $\%U_0$ )	99.65	99.68	99.84	99.23	99.30	99.40	98.62	98.74	99.36
Rel. error, VC w.r.t. AD (%)	0.00	0.00	-0.05	0.08	0.08	-0.02	0.30	0.28	-0.01

Note: Both tools account for the ground effect. A positive relative error indicates that the vortex cylinder model underestimates the induction compared with the actuator disk results.

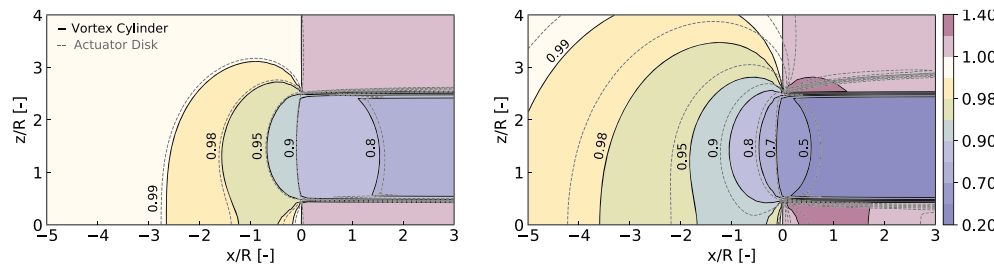


**FIGURE 9** Axial velocity field with ground effect obtained by the vortex cylinder model and actuator disk simulation for two  $C_T$  values. The turbine hub height is located at  $z = 1.5R$ . (Left)  $C_T = 0.40$ ; (right)  $C_T = 0.95$  [Colour figure can be viewed at [wileyonlinelibrary.com](http://wileyonlinelibrary.com)]

at a low-thrust coefficient, and fair at a higher thrust coefficient. The flow is no longer axisymmetric because of the presence of the ground. When compared with Figure 5, it appears that the differences between the two models are more significant when the ground effect is accounted for. The vortex cylinder model appears to underestimate the induction compared with the actuator disk results. The results are further quantified by reporting the relative error between the two models in Table 1. In the table, the results for different hub heights are given:  $H = 1.5R$  (corresponding to Figure 9),  $H = 2R$ , and  $H = \infty$ . The velocity from the actuator disk is taken as a reference and reported at two upstream locations,  $x = -2R$  and  $x = -5R$ , relative to the free-stream velocity,  $U_0$ . The relative error between the vortex cylinder model and the actuator disk are below 0.1% for  $C_T = 0.4$  at both upstream locations. On the other hand, at the high-thrust coefficient, the error is around 1% close to the rotor and 0.3% at  $2.5D$  upstream. The vortex cylinder model slightly underestimates the induction in most cases. This underestimation is mainly attributed to the absence of wake expansion. The results from this table can be used to correct the estimated inductions from the vortex cylinder model accordingly based on the operating condition of the rotor.

### 3.5 | Different contributions from the wake vorticity: wake length and ground effect

One key advantage of vorticity-based methods is the possibility of evaluating the induced velocity from separate parts of the vorticity distribution. In this section, we evaluate the influence of the wake length and the ground effect on the induced velocity. The motivation for studying wake length is based on the fact that the infinite wake length used in the vortex cylinder model is not realistic because the wake will diffuse downstream and extend to a finite length.

The axial induced velocity from a vortex cylinder extending from  $x = 0$  to  $x = L$  is written as  $u_L$ . The analytical formula for the velocity is found in Appendix C1. When the cylinder extends to  $x \rightarrow +\infty$ , the velocity is written as  $u_\infty$ . The expression for  $u_\infty$  is given by Equation 4. The velocity ratio,  $u_L(x)/u_\infty(x)$ , is plotted in Figure 10A for varying wake lengths and at two locations: the rotor plane ( $x = 0$ ) and  $2.5D$  upstream ( $x = -5R$ ). Figure 10A indicates that 90% of the induced velocity at the rotor comes approximately from the first  $2R$  of the wake and 99% from the first  $7R$ . At an upstream location of  $-5R$ , a longer wake ( $L \approx 11R$ ) is necessary to capture 90% of the induced velocity. This is further illustrated in Figure 10B. The near-wake and far-wake regions are defined as the part of the wake located at  $x \leq 10R$  and  $x > 10R$ , respectively. The different

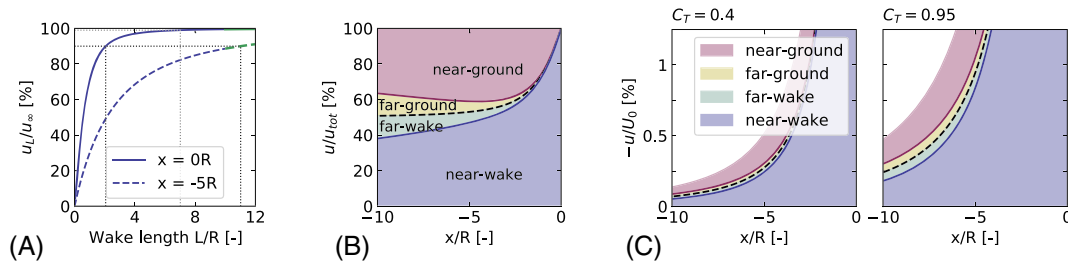


**FIGURE 10** Influence of wake length and ground effect on the axial induced velocity. A, Induced velocity at two  $x$ -locations as a function of wake length. The velocities are normalized by the velocity obtained for a semi-infinite wake. B, Contributions from the ground effect, far-wake, and near-wake to the total induced velocity,  $u_{tot}$ , at different upstream locations. The limit between the near-wake and far-wake is taken as  $x = 10R$ . C, Velocity contributions normalized by the free-stream velocity for  $C_T = 0.4$  and  $C_T = 0.95$  [Colour figure can be viewed at [wileyonlinelibrary.com](http://wileyonlinelibrary.com)]

regions are illustrated in Figure 2. Their induced velocities are written as  $u_{nw}$  and  $u_{fw}$ , respectively, with their sum such that  $u_\infty = u_{nw} + u_{fw}$ . A similar decomposition at  $x = 10R$  is done for the velocity,  $u_g$ , induced by the mirrored semi-infinite cylinder, accounting for the ground effect. The contributions are called “near-ground” and “far-ground,” respectively, with  $u_g = u_{ng} + u_{fg}$ . The total axial induced velocity at any location is thus

$$u_{tot} = u_{nw} + u_{fw} + u_{ng} + u_{fg}. \quad (13)$$

Figure 10B confirms that the relative contribution of the far-wake increases with upstream distance. It also shows that the ground effect contributes to approximately half the induced velocity for upstream distances,  $x < -4R$ . The individual contributions are all proportional to  $\gamma_t$ , and as such, the results do not depend on the thrust coefficient. Yet it is common to think of the velocity upstream of the turbine as the total velocity,  $U = U_0 + u_{tot}$ , in which the relative “loss” of free-stream velocity is then  $-u_{tot}/U_0$ . Expressed this way, the influence of each contribution is put in perspective for different thrust coefficients in Figure 10C. Because a realistic wake is not infinite, it is likely that the semi-infinite model will overestimate the inductions. In Figure 10C, for  $C_T = 0.95$ , the far-wake has a contribution of  $0.1U_0$  at  $x = -10R$ . According to our investigation, it appears that using a length of  $L = 5D$  instead of a semi-infinite cylinder would have almost no impact on the induction zone of a single wind turbine. Yet the wake-length impact will increase when considering wind farms. Additional discussions will follow in Section 5.

### 3.6 | Calibration of the $\gamma_t - C_T$ relationship

The results presented in this section used the relationship given in Equation 3 to determine the vorticity from the thrust distribution. This relationship is taken from the 1D momentum theory and is likely to be approximate.<sup>11</sup> The different actuator disk simulations are used here to calibrate this relationship. Unfortunately, because the vortex cylinder model does not account for wake expansion, a calibration that matches the velocity at the rotor between the two models is not necessarily the one that will minimize the error in the induction zone. Results from the calibration are shown in Figure 11.

- 1D momentum theory ( $\kappa = 1$ ) and Troldborg et al. ( $\kappa = 1.1$ ):

$$\gamma_t = -U_0 \left[ 1 - \sqrt{1 - \kappa C_T} \right], \quad C_T < \kappa. \quad (14)$$

- Calibration to minimize the error in velocity for  $x \in [-5D, -D]$ :

$$\gamma_t = -2U_0 \left[ 0.169C_T + 0.400C_T^2 - 0.482C_T^3 + 0.396C_T^4 \right]. \quad (15)$$

- Calibration to match the rotor center velocity:

$$\gamma_t = -2U_0 \left[ 0.234C_T + 0.143C_T^2 - 0.162C_T^3 + 0.155C_T^4 \right]. \quad (16)$$

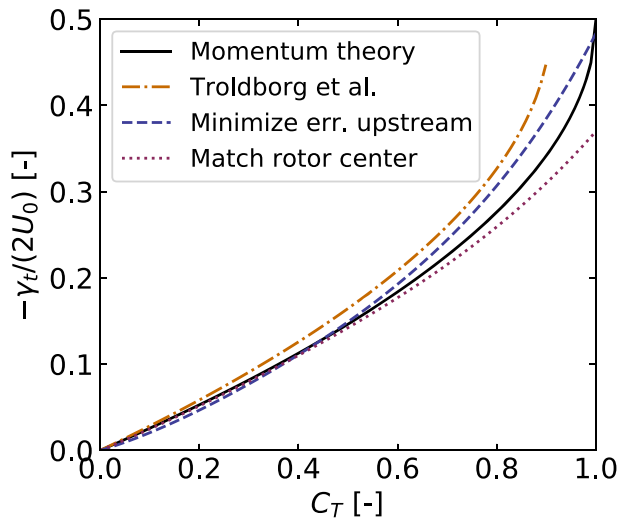


**FIGURE 11** Calibration of the  $\gamma_t - C_T$  relationship using results from actuator disk simulations. We obtained two polynomial fits to minimize the error in the velocity at the rotor center or over the range  $x \in [-5D, -D]$  upstream of the turbine [Colour figure can be viewed at [wileyonlinelibrary.com](http://wileyonlinelibrary.com)]

The figure also presents the formula used by Troldborg et al.<sup>25</sup> for their self-similar model. We observe that minimizing the error in the induction zone requires increasing the vorticity compared with the one that would be obtained from the momentum theory formula. Unfortunately, the calibration works in the opposite direction to match the velocity at the rotor center. This can be understood by considering the curving of the vorticity surface that occurs for the high-thrust coefficient and accompanies wake expansion. For the remaining part of this article, we will use Equation 15.

### 3.7 | Computational time

The vortex cylinder model was implemented in Python, and we ran performance tests on one processor. The computational time of the full-velocity fields ( $\approx 50\,000$  points) about one rotor is approximately 1 s for the vortex cylinder model. The actuator disk simulations were run on multiple processors using a compiled language software, which took approximately 1 and 2 CPU hours for the single rotor cases with and without swirl, respectively. The computational time for a wind farm of 121 turbines and 1 million points (see Figure 14) was 15 min using the vortex cylinder model. Actuator disk simulations for a similar wind farm would require about 200 CPU hours. The vortex cylinder model is then observed to be three orders of magnitude faster in both the single turbine and wind farm cases.

## 4 | WIND FARM BLOCKAGE EFFECT AND PERFORMANCE PREDICTION

In this section, we use the vortex cylinder model to study the blockage effect of wind farms and estimate their power production. Section 4.1 is used to verify the induction part of the vortex cylinder model for a wind farm, using actuator disk results. We use an uncoupled version of the model to compare with actuator disk simulations. The uncoupled approach ensures that the vortex cylinder model uses the same thrust coefficients than the ones obtained in the actuator disk simulations. This is achieved by neglecting the wake coupling presented in Section 2.4, and prescribing the loading of each turbine. In Section 4.2, we perform parametric studies to show the effect of turbine spacing, farm layout, hub-height, and thrust coefficient on the induction zone. An uncoupled approach is again used, this time using  $C_T$  values obtained from the standalone FLORIS framework, to reduce the computational expense of the parametric study. Few actuator disk simulations are run for cross-validation. Last, in Section 4.3, we apply the full coupling methodology presented in Section 2.4, where the vortex cylinder model is integrated into the FLORIS framework. Performance predictions for a fictitious wind farm are provided.

### 4.1 | Comparison of the uncoupled vortex cylinder model with actuator disk simulations

We compare the vortex cylinder model with results from the actuator disk simulations in this section. Further, we investigate different wind farm layouts, as illustrated in Figure 12B. The actuator disk simulations were run using a basic controller to adjust the loading of waked turbines while prescribing the thrust coefficient of the front turbines. The loading extracted from the actuator disk simulation is used to determine the intensity of each vortex cylinder of the vortex cylinder model using Equation 15. The velocity field from each individual vortex cylinder model was

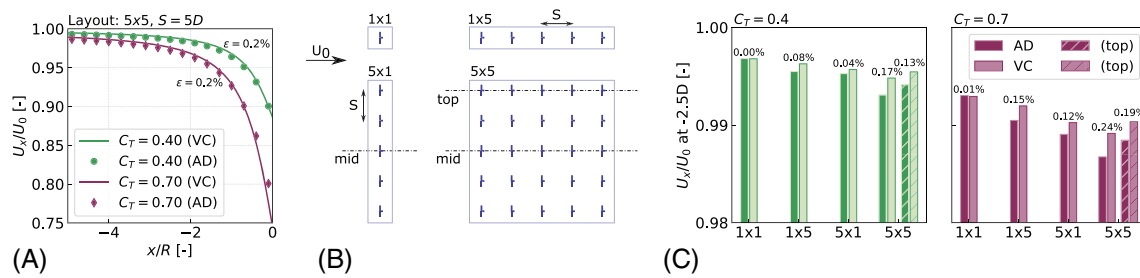


**FIGURE 12** Comparison of the uncoupled vortex cylinder (VC) model against actuator disk (AD) simulations for different wind farm configurations. A, Axial velocity field in the induction zone of the mid row, for the  $5 \times 5$  layout with  $S = 5D$ , and for two  $C_T$  values. The mean relative error,  $\epsilon$ , is reported. B, Sketch of the different layouts considered and definition of the mid and top rows. C, Axial velocity at  $x = -2.5D$  for different layouts and two  $C_T$  values. Hashed bars are at the top row, whereas others are for the mid row. Relative error is reported in % [Colour figure can be viewed at [wileyonlinelibrary.com](http://wileyonlinelibrary.com)]

superposed to each other to obtain the full velocity field according to Equation 12. This uncoupled approach is thereby used to verify the accuracy of the induction model for a wind farm. All the results presented in this section are for a hub height of  $z = 1.5R$ . Figure 12 provides a comparison of the results between the vortex cylinder and actuator disk models. The velocity field obtained by the vortex cylinder model for a  $5 \times 5$  layout is in good agreement with the actuator disk simulations, as shown in Figure 12A. The mean relative error in the induction zone in front of the “mid” row is 0.2% for both thrust coefficients. Figure 12C provides a closer look at the velocity at  $x = -2.5D$  for different layouts. The vortex cylinder model follows the same trend as the actuator disk simulations: (1) the velocity in front of the mid row is reduced, as more turbines are introduced in the farm, (2) the  $5 \times 1$  layout has more influence than a  $1 \times 5$  layout,\*\* and (3) the top row shows less velocity reduction. We observe that the vortex cylinder model systematically underestimates the induced velocity, which is surprising because the model used an infinite wake length. This underestimation can likely be attributed to the absence of wake expansion. More discussions follow in Section 5.

## 4.2 | Assessment of the wind farm blockage effect using the uncoupled vortex cylinder model

We investigated a limited set of wind farm configurations in Section 4.1. From there, we ran the FLORIS framework for different layouts using the thrust curve from the National Renewable Energy Laboratory (NREL) 5-MW<sup>41</sup> wind turbine. For each layout, the converged thrust coefficient of each turbine was extracted, and the loading was used as input to the vortex cylinder model to compute the induction field. A small error is introduced by using the uncoupled approach, at the benefit of having a lower computational cost than the fully coupled methodology presented in Section 2.4. The axial velocity obtained at  $x = -2.5D$  for different layouts, turbine spacing, thrust coefficients, and hub heights is plotted in Figure 13. We note that the thrust coefficient reported is for the first row of turbines—downstream turbines are operating at different conditions, which is a function of the turbine design and controller strategy. Figure 13 shows that the blockage effect is increased with decreased turbine spacing, increased thrust coefficient, increased farm size, and reduced hub height. For the range of parameters considered, the vortex cylinder model predicts that the axial velocity at  $2.5D$  upstream of a wind farm may easily be reduced by 2%.

## 4.3 | Wind farm flow field using the coupled vortex cylinder/FLORIS model

In this section, we apply the coupling methodology presented in Section 2.4 using the FLORIS model for the wake computation and the current vortex cylinder model for the induction. The source code for this coupling, with test cases and examples, is made available online as part of the WIZ package.<sup>28</sup> Sample results are provided in Figure 14 for a square layout of  $5 \times 5$  wind turbines and the layout Danish Anholt wind farm. Rather than using turbine data from the manufacturer, we used the NREL 5-MW wind turbine. The figure shows that realistic flow fields are obtained, and the simple induction/wake velocity merging appears satisfactory. Yet the merging procedure cannot enforce continuity, a limitation that is discussed in Section 5.

An application example concludes this section. The coupled vortex cylinder/FLORIS code was run for the Anholt layout (with the fictitious NREL 5-MW turbine), for a set of wind speeds and wind directions, and with or without the induction model. The relative difference in total power production, with or without the accounting for induction, is reported in Figure 15. The algorithm was run using three and five iterations, to assess the convergence of the method. No significant differences were found between the two simulation sets, indicating that 3 iterations are likely sufficient to obtain convergence of the thrust and power coefficients within the farm. From Figure 15, we observe that this particular layout

\*\*This result is mostly expected from the  $1/r^2$  influence of the vorticity, but it also depends on the vortex intensity of the waked turbines.

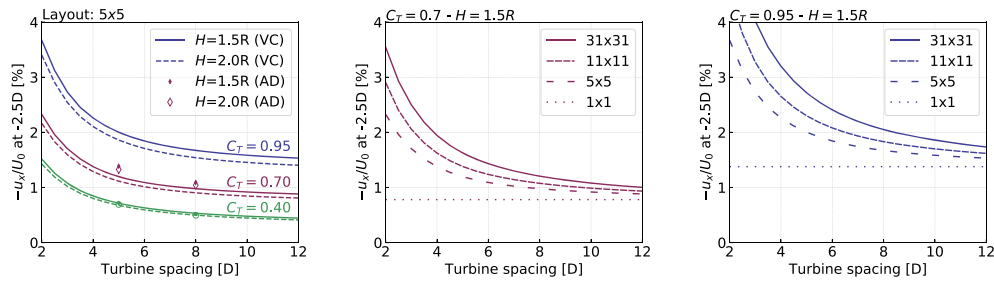


**FIGURE 13** Influence of turbine spacing on the induction at 2.5D upstream of a wind farm, and on the wind farm centerline using the vortex cylinder (VC) model. Left: influence of thrust coefficient, and distance to the ground for a layout of  $5 \times 5$ . Actuator disk (AD) simulations are presented using markers when available. Center and right: influence of wind turbine spacing and layout, for  $H = 1.5R$  and for  $C_T = 0.7$  and  $C_T = 0.95$  [Colour figure can be viewed at [wileyonlinelibrary.com](http://wileyonlinelibrary.com)]

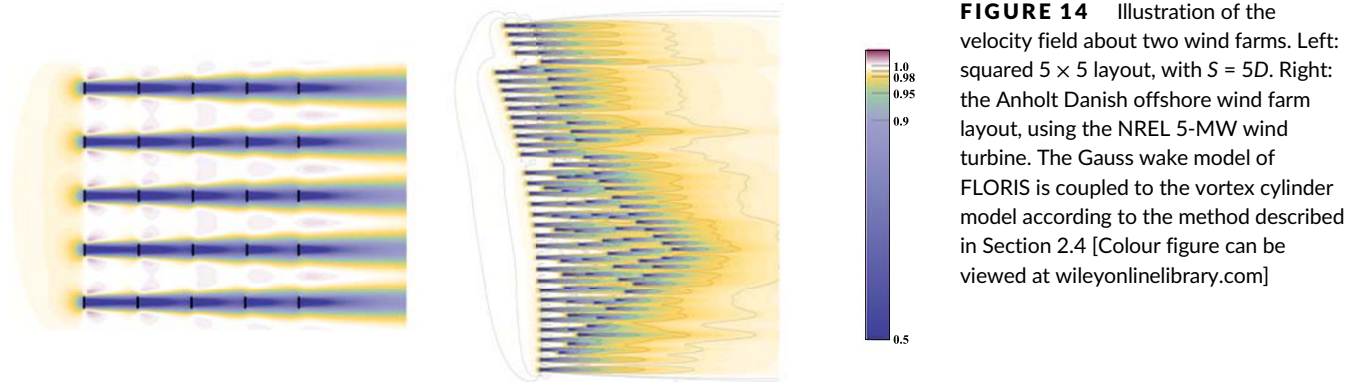


**FIGURE 14** Illustration of the velocity field about two wind farms. Left: squared  $5 \times 5$  layout, with  $S = 5D$ . Right: the Anholt Danish offshore wind farm layout, using the NREL 5-MW wind turbine. The Gauss wake model of FLORIS is coupled to the vortex cylinder model according to the method described in Section 2.4 [Colour figure can be viewed at [wileyonlinelibrary.com](http://wileyonlinelibrary.com)]

with this particular turbine is mainly sensitive to the induction effect for the north and south sectors. At high-thrust coefficients ( $U_0 = 5$  m/s), the power production is reduced by approximately 0.2% when induction effects are included and the wind comes from the southern sector. For other wind directions, the power reduction is below 0.1% and below 0.02%, for the most part. The low power reduction observed in this example may be attributed to the use of a large power rating (5 MW) compared with the designed rating of 3.6 MW. Interestingly, a small power increase is observed for the east and west sectors at  $U_0 = 12$  m/s. This increase may be attributed to the speed-up effect provided by the induction model when wind turbines are located close to each other in the direction orthogonal to the flow.

## 5 | DISCUSSION AND FUTURE WORK

The previous sections demonstrated that the vortex cylinder model can be used as an engineering model to obtain velocity fields within wind farms with remarkable accuracy and at a negligible computational cost. Several limitations of the method are discussed in this section to pave the way for future work. Most of the points that are raised apply to the vortex cylinder model, but often, to the engineering wake models as well.

### 5.1 | Actuator disk simulations as reference

Results from actuator disk simulations were used as a reference to assess the quality of the velocity field obtained from the vortex cylinder model. This raises the question of the validity of the RANS model and its suitability for such study. The employed RANS actuator disk setup has been previously validated against lidar measurements of the induction zone in front of a full-scale wind turbine.<sup>24</sup> Turbulence modeling is a source of variability of CFD results. Here, the  $k - \omega$  shear stress transport (SST) turbulence model was used for turbulence closure; however, the maximum impact of changes in the turbulence model parameters was shown to be of 0.1% with respect to the velocity obtained with inviscid computations.<sup>42</sup> In the same study, comparison with actuator line simulations showed that the signature of individual blades in the induction zone is lost with time-averaging. From these results, the use of an actuator disk representation of the rotor appears fair. Similar observations were made by Troldborg et al.<sup>25</sup> Yet for a tightly spaced wind farm, the influence of the turbine design will gain importance, and actuator line CFD may be considered.

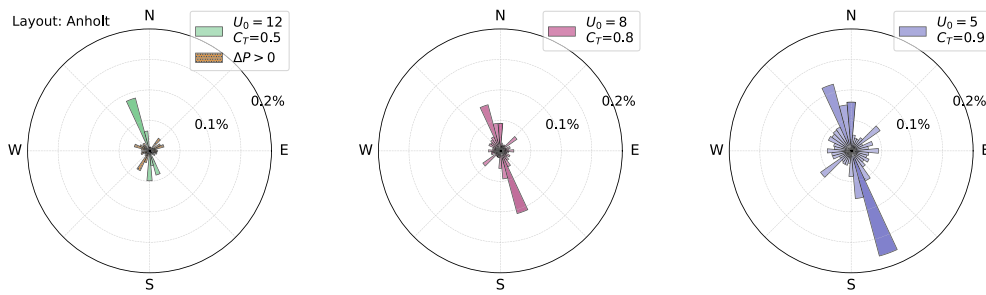


**FIGURE 15** Difference in total power production ( $\Delta P$ ) when accounting for induction effects and using the Anholt layout. Unless indicated, the bars represent a decrease in power  $\Delta P < 0$ . From left to right, the wind speed is 12, 8, and 5 m/s, respectively, resulting in different  $C_T$  values. Twenty-four wind directions are used on each plot. In most cases, including the induction effect decreases the power ( $\Delta P < 0$ ), except for the east (E) and west (W) sectors at  $U_0 = 12$  m/s [Colour figure can be viewed at [wileyonlinelibrary.com](http://wileyonlinelibrary.com)]

## 5.2 | Near-wake and far-wake expansion

The omission of near-wake expansion is the main source of discrepancies between actuator disk and vortex cylinder results. The vorticity and momentum formulations of an actuator disk are two equivalent formulations. Yet the vortex model presented in this work is an approximation of the vortex actuator disk that does not account for wake expansion. Accounting for this effect in the model would then improve the predictive performance. The approach would consist of modeling the wake surface as a discrete set of rings of varying radii (see, e.g., previous studies<sup>1,11,43</sup>). To simplify the computation, the near-wake expansion can be computed analytically using Equation 7 and the conservation of mass, as done in Chapter 15 of Branlard.<sup>33</sup> The use of vortex doublets in the far-wake can be used to speed up the computation. In spite of this source of discrepancy, it appears that the actuator disk and vortex cylinder results are in strong agreement, in particular for low-to-medium  $C_T$ , and the benefit of adding near-wake-expansion will likely be limited.

The term “far-wake expansion” refers to the expansion that results from the wake meandering. The meandering effectively diffuses the time-averaged wake, similar to random-walk diffusion. Engineering wake models usually include such expansion. Hence, the coupled wake/induction model partially includes this effect because the loading of waked turbine is obtained based on the expanded wake. To be consistent, the induction zone should also be a “meandered” induction zone, resulting from a time-averaged induction zone obtained over a period where the wake is meandering. This meandered induction zone would be of reduced intensity compared with the one obtained with a straight wake. As mentioned in a following paragraph, the impact of turbulence on the induction zone was observed to be limited in other studies.<sup>42</sup>

## 5.3 | High thrust

Different considerations are required for large thrust coefficient values (e.g.,  $C_T > 1$ ). First, the 1D momentum result,  $a = \frac{1}{2} [1 - \sqrt{1 - C_T}]$ , becomes invalid. This equation was used in Equations 1 and 3, but alternative formulae were presented in Figure 11. It can also be corrected using any of the high-thrust corrections typically used in blade element momentum implementations, such as the Glauert or Spera corrections (see, e.g., Hansen<sup>44</sup>). Additional details on how to apply the Spera correction to Equation A3 are given in Branlard and Gaunaa.<sup>4</sup> The second issue that arises is that for high thrust, the wake becomes turbulent and the aerodynamics will change<sup>39</sup>: the average wake vorticity surface will expand and rapidly collapse toward the rotor axis, which the current model does not capture. The induction zone will be influenced by two counteracting effects: the wake vorticity surface will be strong (resulting in higher inductions), but the wake surface will also diffuse faster (resulting in less induction). Similar issues exist for wake profiles, and hence, engineering wake models. Therefore, additional work is needed to study the challenging case of the unsteady wakes under high-thrust loading.

## 5.4 | Turbulence, diffusion, and wake length

Wake-added turbulence and atmospheric turbulence are accounted for by wake models but omitted in the vortex cylinder model. Turbulence will diffuse the wake vorticity, thereby reducing the strength of the vorticity sheet. The average vorticity field will be similar to the one from the vortex cylinder model, but with a vorticity distribution ( $\gamma_t$ ) that decreases with the downstream distance, effectively reducing the induction zone. From this consideration, it may be expected that the vortex cylinder model overestimates the induction zone under turbulent flows. Comparisons with turbulent simulations can be performed to tune the vorticity strength  $\gamma_t$  as a function of turbulence intensity. It is expected that this simple scaling approach will provide a sufficiently accurate description of the induction zone. To further improve the model, it would also be possible to

define  $\gamma_t(x)$ , which would be diffused downstream based on an eddy viscosity parameter, and then compute the velocity field using a discrete set of vortex rings or doublets placed along the  $x$ -axis. This approach would be computationally more expensive and might not justify the effort; the impact of turbulence on the induction zone was observed to be limited in the work from Meyer Forsting.<sup>42</sup>

In light of the results presented in Figure 10, the impact of using an infinite wake compared with a finite wake appears limited. It was originally anticipated that the model with an infinite wake would overestimate the induction zone. Yet the results from Figure 12 revealed that the vortex cylinder model systematically underestimates the induction compared with actuator disk simulations. The source of discrepancy is likely to be the absence of near-wake expansion because it is the only fundamental difference between the models. As a result, it appears that using a finite wake length is unnecessary because it would lead to a greater underestimation. The consideration of the wake length may still be relevant for tuning the model for high-thrust configurations or turbulent inflows. The formulae for a wake of finite length are provided in Appendix C1.

## 5.5 | Interaction with the boundary layer

In this study, we did not consider large-scale array effects and the two-way interaction of the wind turbines with the atmospheric boundary layer (see, e.g., Allaerts et al.<sup>45</sup>). Ground effect was accounted for, but not the effect of shear. The vorticity associated with shear will interact with the wake vorticity and result in a different wake shape than the assumed vortex cylinder. Stability will also have an impact on how the wake diffuses and rolls up downstream, eventually leading to a different wake shape than the one assumed. The wake length discussed in the previous paragraph may be adapted based on the stability conditions, using longer wakes for stable conditions. The source of errors, associated with the omission of the interaction between the wake and the boundary layer, are likely to increase for turbines further downstream within a wind farm. Therefore, the current model may need further investigation because it is not expected to capture deep-array effects. Yet the authors do not expect shear to significantly affect the results provided for the induction zone of a single turbine (or the front column of a wind farm), because the main effect is captured by the ground effect: the induction field can then be superposed to a constant shear profile  $U_0(z)$  (see, e.g., Meyer Forsting et al.<sup>42</sup>).

## 5.6 | Inconsistency between wake models and the vortex cylinder model

The methodology presented in Section 2.4 relied on simple approximations to couple the wake and vortex cylinder models. The solution presented falls within the realm of engineering models and leaves room for improvement. Engineering wake models are typically valid after the pressure has recovered in the wake, about 2 to 3D downstream of the rotor, and after the near-wake expansion has reached its maximum. In a framework such as FLORIS, the wake models are applied as early as 0D. Hence, the velocity fields from the vortex cylinder model and wake models will be inconsistent, and noncontinuous at the rotor. The implementation of near-wake models to transition between the rotor flow and the fully developed wake would reduce these discontinuities.

In a similar work<sup>†</sup>, Nygaard et al.<sup>46</sup> set the flow induced by vortex cylinders to zero in the half-domain behind each rotor (see footnote in Section 2.4). The authors argue that current wake models have been tuned against measurements that inherently include some induction effects. Recalibration of wake models may thereby be needed for further tuning of the coupling algorithm.

In general, the main integration issue comes from the fact that engineering wake models are expressed in terms of velocity. Formulating these models using vorticity would fully integrate the induction and wake models, leading to a uniform and continuous formulation of the velocity field. An alternative would be to correct the wake velocity field such that mass is conserved (i.e., projecting the field onto a divergence-free field), which would then also provide the induction field.

## 6 | CONCLUSIONS

A novel methodology to compute wind farm velocity fields and wind farm production was presented, with the aim of accounting for wind farm blockage effects. This engineering model, based on a vortex cylinder, displays remarkable accuracy at a low computational cost. The wind turbine and wind farm blockage effects determined with the analytical vortex cylinder model agree to a high degree with the ones from the actuator disk simulations at moderate thrust coefficients. The agreement remains fair but progressively deteriorates as the thrust coefficient increases because of the absence of wake expansion in the vortex cylinder model. The model successfully captures the ground effect by using a mirrored vortex model. The main features of the flow are captured by the model for different layouts and locations

<sup>†</sup>The authors from the current work and the authors of the work presented in one study<sup>46</sup> have been exchanging on the topic, which explains the similarity of some of the methods presented. We are grateful for this dialog, and the authors would particularly like to thank Nicolai Nygaard for his feedback on this article.

upstream of the wind farm (e.g., at the middle or first row). Though moderate, a systematic underestimation of the induction predicted by the vortex cylinder model was observed. Corrections may be derived to account for the small underestimation reported in this work. Overall, we observed fair agreement between the vortex cylinder model and the actuator disk simulations, with relative errors typically around 0.2%. The computational time of the vortex cylinder model is three orders of magnitude smaller than the actuator disk simulations, allowing fast estimates of the induction zone with a satisfying accuracy.

The model predicts that wind speed measured at  $2.5D$  upstream of a wind farm may typically be reduced by 2% compared with the undisturbed velocity, which will affect the determination of the wind farm energy yield. The flow modeling of wind farm prediction tools can be improved by using the methodology presented in this work. An example of application for a given wind farm—using the FLORIS framework—showed that wind farm power production was reduced between 0.02% and 0.2% when the induction effect was accounted for.

The source code and data for the results presented in this article are available in a public repository. Future work will focus on investigating the model for different turbulence and stability conditions and performing validations against field measurements.

## ORCID

Emmanuel Branlard  <https://orcid.org/0000-0002-7750-6128>

Alexander R. Meyer Forsting  <https://orcid.org/0000-0002-3133-1860>

## REFERENCES

- Meyer Forsting AR, Troldborg N, Gaunaa M. The flow upstream of a row of aligned wind turbine rotors and its effect on power production. *Wind Energy*. 2017;20(1):63-77.
- Rankine WJ. On the mechanical principles of the action of propellers. *Trans Inst Nav Archit*. 1865;6:13.
- Joukowski NE. Vortex theory of screw propeller, I. *Trudy Otdeleniya Fizicheskikh Nauk Obshchestva Lubitelei Estestvoznaniya*. 1912;16(1):1-31. (in Russian). French translation in: *Théorie tourbillonnaire de l'hélice propulsive*. Gauthier-Villars: Paris, 1929; 1: 1-47.
- Branlard E, Gaunaa M. Superposition of vortex cylinders for steady and unsteady simulation of rotors of finite tip-speed ratio. *Wind Energy*. 2015a;19(7):1307-1323. <https://doi.org/10.1002/we.1899>
- Glauert H. *Airplane Propellers, Division L*. W.F. Durand (ed). Berlin: Julius Springer; 1935.
- Branlard E, Gaunaa M. Cylindrical vortex wake model: right cylinder. *Wind Energy*. 2014;524(1):1-15.
- Branlard E, Gaunaa M. Cylindrical vortex wake model: skewed cylinder, application to yawed or tilted rotors. *Wind Energy*. 2015b;19(2):345-358.
- Medici D, Ivanell S, Dahlberg J-A, Alfredsson PH. The upstream flow of a wind turbine: blockage effect. *Wind Energy*. 2011;14:691-697.
- Snel H, Schepers JG. Joint investigation of dynamic inflow effects and implementation of an engineering method. ECN-C-94-107, Energy Research Centre of the Netherlands, Petten; 1995.
- Yu W, Tavernier D, Ferreira CS, van Kuik GAM, Schepers G. New dynamic-inflow engineering models based on linear and nonlinear actuator disc vortex models. *Wind Energy*. 2019;22(11):1433-1450. <https://doi.org/10.1002/we.2380>
- van Kuik GAM, Lignarolo LEM. Potential flow solutions for energy extracting actuator disc flows. Submitted to *Wind Energy*; 2015.
- Yu W, Ferreira CS, van Kuik GAM, Baldacchino D. Verifying the blade element momentum method in unsteady, radially varied, axisymmetric loading using a vortex ring model. *Wind Energy*. 2017;20(2):269-288. <https://doi.org/10.1002/we.2005>
- Bontempo R, Manna M. A ring-vortex free-wake model for uniformly loaded propellers. part i-model description. *Energy Procedia*. 2018;148:360-367. ATI 2018 - 73rd Conference of the Italian Thermal Machines Engineering Association.
- Leuthold R, Crawford C, Gros S, Diehl M. Engineering wake induction model for axisymmetric multi-kite systems. *J Phys: Conf Ser*. 2019;1256:012009. <https://doi.org/10.1088/1742-6596/1256/1/012009>
- Pedersen MD. Steady and transient inflow dynamics with actuator disk vortex theory. *Wind Energy*. 2019;22(1):124-139.
- Shapiro CR, Gayme DF, Meneveau C. Filtered actuator disks: theory and application to wind turbine models in large eddy simulation. *Wind Energy*. 2019;22:1414-1420.
- Branlard E, Meyer Forsting A. Using a cylindrical vortex model to assess the induction zone in front of aligned and yawed rotors. In: *Proceedings of EWEA Offshore 2015 Conference*; 2015.
- Mitraszewski K, Hansen KS, Nygaard N, Réthoré P-E. Empirical investigation of wind farm blockage effects in horn rev 1 offshore wind farm. In: *Proceedings of the science of making torque from wind conference 2012*; 2012.
- Asimakopoulos M, Clive P, Boddington R. Offshore compression zone measurement and visualization. *Proceedings of the European Wind Energy Association 2014 Annual Event (Barcelona, Spain)*; 2014.
- Simley E, Pao LY, Gebraad P, Churchfield M. Investigation of the impact of the upstream induction zone on lidar measurement accuracy for wind turbine control applications using large-eddy simulation. *J Phys: Conf Ser*. 2014;524(1):012003.
- Howard KB, Guala M. Upwind preview to a horizontal axis wind turbine: a wind tunnel and field-scale study. *Wind Energy*. 2016;19(8):1371-1389. <https://doi.org/10.1002/we.1901>
- Nishino T, Draper S. Local blockage effect for wind turbines. *J Phys Conf Ser*, 625; 2015.
- Bleeg J, Purcell M, Ruisi R, Traiger E. Wind farm blockage and the consequences of neglecting its impact on energy production. *Energies*. 2018;11(6):1609.
- Meyer Forsting AR, Troldborg N, Murcia Leon JP, Sathe A, Angelou N, Vignaroli A. Validation of a cfd model with a synchronized triple-lidar system in the wind turbine induction zone. *Wind Energy*. 2017;20:1481-1498.
- Troldborg N, Meyer Forsting AR. A simple model of the wind turbine induction zone derived from numerical simulations. *Wind Energy*. 2017;20(12):2011-2020. <https://doi.org/10.1002/we.2137>
- Meyer Forsting AR, van der Laan MP, Troldborg N. The induction zone/factor and sheared inflow: a linear connection? *J Phys: Conf Ser*. 2018;1037:072031. <https://doi.org/10.1088/1742-6596/1037/7/072031>

27. McTavish S, Rodrigue S, Feszty D, Nitzsche F. An investigation of in-field blockage effects in closely spaced lateral wind farm configurations. *Wind Energy*. 2014;18:1989-2011.
28. Branlard E. Wiz, wake and induction zone model. <https://github.com/ebranlard/wiz>; 2019.
29. Burton T, Sharpe D, Jenkins N, Bossanyi E. *Wind energy handbook*. first. New-York, N.Y.: J. Wiley & Sons; 2002. <https://doi.org/10.1002/0470846062>
30. van Kuik GAM. On the generation of vorticity by force fields in rotor- and actuator flows. *Renew Energy*. 2014;70:124-128. <https://doi.org/10.1016/j.renene.2014.02.056>
31. Coleman RP, Feingold AM, Stempin CW. Evaluation of the induced-velocity field of an idealized helicopter rotor. NACA ARR No. L5E10 1-28; 1945.
32. Branlard E, Gaunaa M, Machefaux E. Investigation of a new model accounting for rotors of finite tip-speed ratio in yaw or tilt. *J Phys: Conf Ser*. 2014; 524(1):1-11. <https://doi.org/10.1088/1742-6596/524/1/012124>
33. Branlard E. *Wind turbine aerodynamics and vorticity-based methods: Fundamentals and recent applications*. New York: Springer International Publishing; 2017. <https://doi.org/10.1007/978-3-319-55164-7>
34. Annoni J, Fleming P, Scholbrock A, Dana S, Adcock C, Porte-Agel F, Raach S, Haizmann F, Schilpf D. Analysis of control oriented wake modeling tools using lidar field results. *Wind Energy Sci*. 2018;3:819-831.
35. Michelsen JA. Block Structured Multigrid solution of 2D and 3D elliptic PDE's. AFM 94-05 - Department of Fluid Mechanics, Technical University of Denmark; 1994.
36. Sørensen NN. General purpose flow solver applied to flow over hills. *Ph.D. Thesis*: Risø National Lab., Roskilde (Denmark). Meteorology and Wind Energy; Danmarks Tekniske Univ., Lyngby (Denmark); 1995.
37. Réthoré P-E, Sørensen NN. A discrete force allocation algorithm for modelling wind turbines in computational fluid dynamics. *Wind Energy*. 2012;15: 915-926.
38. Troldborg N, Sørensen NN, Réthoré P-E, van der Laan P. A consistent method for finite volume discretization of body forces on collocated grids applied to flow through an actuator disk. *Comput Fluids*. 2015;119:197-203.
39. Martinez-Tossas LA, Branlard E, Shaler K, Vijayakumar G, Ananthan S, Sakievich P, Jonkman J. Wind turbine wakes: High-thrust coefficient. *Wind Energy*. (under review) 2020.
40. Madsen H, Bak C, Døssing M, Mikkelsen R, Øye S. Validation and modification of the blade element momentum theory based on comparisons with actuator disc simulations. *Wind Energy*. 2010;13:p373-389.
41. Jonkman J, Butterfield S, Musial W, Scott G. Definition of a 5-MW reference wind turbine for offshore system development. NREL/TP-500-38060, National Renewable Energy Laboratory; 2009.
42. Meyer Forsting AR, Troldborg N, Bechmann A, Réthoré P-E. Modelling wind turbine inflow: the induction zone. *Ph.D. Thesis*. Denmark: Department of Wind Energy Aerodynamic design; 2017.
43. Øye S. A simple vortex model of a turbine rotor. In: Proc. of the third IEA symposium on the aerodynamics of wind turbines, etsu, harwell; 1990: 4.1-1.15.
44. Hansen MOL. *Aerodynamics of Wind Turbines—Second Edition*. London, Sterling, VA: Earthscan; 2008.
45. Allaerts D, Broucke SV, van Lipzig N, Meyers J. Annual impact of wind-farm gravity waves on the belgian-dutch offshore wind-farm cluster. *J Phys: Conf Ser*. 2018;1037:072006. <https://doi.org/10.1088/1742-6596/1037/7/072006>
46. Nygaard NG, Steen ST, Poulsen L, Pedersen JG. Modelling cluster wakes and wind farm blockage. *J Phys: Conf Ser*. 2020.
47. Gribben BJ, Hawkes GS. A potential flow model for wind turbine induction and wind farm blockage, Frazer-Nash Technical Paper; 2019.

**How to cite this article:** Branlard E, Meyer Forsting AR. Assessing the blockage effect of wind turbines and wind farms using an analytical vortex model. *Wind Energy*. 2020;1-19. <https://doi.org/10.1002/we.2546>

## APPENDIX A: SUPERPOSITION OF ELEMENTARY MODELS FOR FINITE TIP-SPEED RATIOS

The model presented in this work can be further improved by using a superposition of elementary models, of intensity  $\gamma_t(r)$ , as illustrated in Figure 1D). The spanwise distribution of vorticity corresponds to a spanwise distribution of loading, thereby accounting for finite tip-speed ratio and wake swirl<sup>††</sup> and providing a finer description of the rotor loads and flow field. The vorticity strengths are determined from the spanwise distribution of the thrust coefficient according to the method described in Branlard and Gaunaa,<sup>4</sup> which is repeated in this section. The local thrust coefficient,  $C_t(r)$ , is assumed to be known. The corresponding bound circulation along the span,  $\Gamma$ , is determined at each radial position by solving Equation A1 for  $k_\Gamma$ :

$$\text{for each } r \in [0, R], \text{ find } k_\Gamma(r) \in [0, 2] \text{ such that, } C_t(r) = k_\Gamma(r) \left( 1 + \frac{k_\Gamma(r)}{4\lambda_r^2} \right), \quad (\text{A1})$$

where  $k_\Gamma$  and  $\lambda_r$  are the dimensionless circulation and the local tip-speed ratio, respectively, defined as

$$k_\Gamma(r) = \frac{\Omega \Gamma(r)}{\pi U_0^2}, \quad \lambda_r = \frac{\Omega r}{U_0}, \quad (\text{A2})$$

where  $\Omega$  is the rotational speed of the rotor. The tangential and axial induction factors are obtained as

$$a'(r) = \frac{k_\Gamma(r)}{4\lambda_r^2}, \quad a(r) = \frac{1}{2} \left[ 1 - \sqrt{1 - C_{t,\text{eff}}} \right], \quad \text{with, } C_{t,\text{eff}} = k_\Gamma(r) [1 + a'(r)] - 8 \int_{r/R}^1 [\lambda_r a'(r)]^2 \frac{dr}{r}. \quad (\text{A3})$$

The helical pitch of the wake,  $h$ , formed by the combination of the two tip-vorticity components,  $\gamma_t$  and  $\gamma_l$ , is obtained as

$$h(r) = \frac{2\pi U_0 [1 - 2a(r)]}{\Omega [1 + 2a'(r)]}. \quad (\text{A4})$$

The intensity of the wake vorticity surfaces is obtained as

$$\gamma_t(r) = -\frac{\cos\chi d\Gamma(r)}{h(r) dr}, \quad \gamma_l(r) = \frac{1}{2\pi r h(r)} \frac{d\Gamma(r)}{dr}. \quad (\text{A5})$$

This method is critical for the accuracy of the vortex cylinder model or other helical vortex wake models. For a typical wind turbine operation condition,  $\gamma_t$  is positive toward the root, and negative toward the tip.

In a numerical implementation, the thrust coefficient and the bound circulation are known at  $n$  finite locations,  $r_i$ , with  $i = 1 \dots n$ , and a discrete number of vortex cylinders are used. The intensity of each vortex cylinder is determined such that

$$\gamma_{t,j} = \int_{r_i}^{r_{i+1}} \gamma_t(t) dr \approx -\cos\chi \frac{\Gamma_i - \Gamma_{i+1}}{h_i}, \quad \text{with } \Gamma_{n+1} = 0. \quad (\text{A6})$$

The velocity field is determined using a linear superposition of the elementary velocity fields induced by each vortex cylinder of radius  $\frac{r_i + r_{i+1}}{2}$  and intensity  $\gamma_{t,i}$ :

$$\mathbf{U} = \mathbf{U}_0 + \mathbf{u}_{\text{superp}}, \quad \text{with } \mathbf{u}_{\text{superp}}(\mathbf{x}) = \sum_{i=1}^n \mathbf{u}_{\text{elem}} \left( \mathbf{x}, R = \frac{r_i + r_{i+1}}{2}, \gamma_t = \gamma_{t,i} \right). \quad (\text{A7})$$

The superposition is only relevant for flows close to the rotor, and consequently, the far-field approximation is irrelevant for such situations.

<sup>††</sup>The elementary model with swirl leads to a singular azimuthal velocity at the root. Hence, infinite tip-speed ratios are implicitly implied when a single vortex cylinder is used. Yet the singularity in the azimuthal velocity is linked to the root vortex, and not to the tip vorticity  $\gamma_t$ . The singularity is removed when considering a superposition of models, with a realistic loading that drops to zero toward the root. Additional discussions are found in Branlard and Gaunaa.<sup>4</sup>

## APPENDIX B: FAR-FIELD APPROXIMATION OF THE VORTEX CYLINDER MODEL

Approximations of the vortex cylinder models are convenient to speed up the computation of the velocity field introduced in Section 2.2. In this article, we derive an approximation based on a vortex doublet formulation that matches the far-field of a vortex cylinder exactly. A different approximation is, for instance, found in the work of Gribben and Hawkes,<sup>47</sup> referred to as the “half-body” approximation. The far-field of the semi-infinite vortex cylinder is equivalent to the continuous distribution of vortex doublets along a semi-infinite line. The far-field equivalence follows directly from the approximation of a vortex ring by a point doublet, as illustrated in Figure B1.

The velocity field induced at a point,  $\mathbf{x}$ , by a point doublet centered on  $(x_0, y_0, 0)$ , of intensity  $m_x$  directed along  $x$ , is<sup>33</sup>

$$u_x(\mathbf{x}) = \frac{3m_x}{4\pi} \left[ \frac{(x-x_0)^2}{\rho_0^5} - \frac{1}{3\rho_0^3} \right], u_y(\mathbf{x}) = \frac{3m_x}{4\pi} \left[ \frac{(x-x_0)(y-y_0)}{\rho_0^5} \right], u_z(\mathbf{x}) = \frac{3m_x}{4\pi} \left[ \frac{(x-x_0)z}{\rho_0^5} \right], \rho_0^2 = (x-x_0)^2 + z^2 + (y-y_0)^2 \quad (\text{B1})$$

The doublet intensity,  $m_x$ , is related to the intensity of a vortex ring,  $\Gamma$ , as  $m_x = \pi R^2 \Gamma$ . The continuous distribution of doublet follows the vortex cylinder center line defined by  $(x, y = mx, z = 0)$ , where  $m = \tan\chi$  is the tangent of the skew angle. The doublet distribution has an intensity of  $dm_x/dx = \pi R^2 \gamma_t$ . Integrating Equation B1 from  $x_0 = 0$  to  $+\infty$ , with  $y_0 = mx_0$ , provides the velocity field induced by the semi-infinite doublet line:

$$u_x(\mathbf{x}) = \frac{\gamma_t R^2}{4} [x^2 l_{50} - 2x l_{51} + l_{52} - l_{30}], u_y(\mathbf{x}) = \frac{\gamma_t R^2}{4} [xy l_{50} + m l_{52} - (mx + y) l_{51}], u_z(\mathbf{x}) = \frac{\gamma_t R^2}{4} [xz l_{50} - z l_{51}] \quad (\text{B2})$$

with

$$l_{30} = \frac{1}{a(ac-b)}, l_{50} = \frac{2ac-b}{a^3(ac-b)^2}, l_{51} = \frac{1}{a(ac-b)^2}, l_{52} = \frac{1}{c(ac-b)^2}, a^2 = x^2 + y^2 + z^2, b = my + x, c^2 = 1 + m^2.$$

The formulae are singular on the doublet line (i.e., for points  $(x, mx, 0)$  with  $x > 0$ ). In the particular case of  $m = 0$ , Equation B2 reduces to

$$(\text{for } m=0, r>0) \quad u_x(x, r) = \frac{\gamma_t R^2}{4} \frac{1}{r^2} \left[ \frac{x^3}{\rho^3} - \frac{x}{\rho} \right], u_r(x, r) = -\frac{\gamma_t \rho R^2}{4} \frac{1}{\rho^3}, \text{ with } \rho^2 = r^2 + x^2, r^2 = y^2 + z^2 \quad (\text{B3})$$

$$(\text{for } m=0, r=0) \quad u_x(x, 0) = \frac{\gamma_t R^2}{4} \frac{1}{x^2}, u_r(x, 0) = 0. \quad (\text{B4})$$

The comparison of Equations 6 and B4 confirms the equivalence of the two velocity fields at infinity upstream. The application of Equation 6 shows that the doublet velocity field approximates the one from the vortex cylinder with an accuracy of 3% at  $x = -6R$ . In this study, the far-field formulae from Equation B2 are used for upstream distances,  $x < -6R$ . This greatly speeds up the calculation of the velocity field from the elementary model because it removes the difficult integration over the azimuth. The far-field formulae may also be applied to a cylinder of finite length. The results are provided in Appendix C1.

## APPENDIX C: FORMULAE OF THE VORTEX CYLINDER MODEL FOR A FINITE WAKE LENGTH

The velocity induced by a cylinder of finite length,  $L$ , may be obtained by summing the velocity field from two semi-infinite vortex cylinders that are shifted by a distance,  $L$ , along the cylinder axis. The equations given in Appendix B1 and Section 2.2 may thus be used to obtain the velocities induced by a finite cylinder. Alternatively, the formulae obtained from direct integration are provided in this section. The velocity induced by a straight vortex cylinder extending from  $x = 0$  to  $x = L$  is

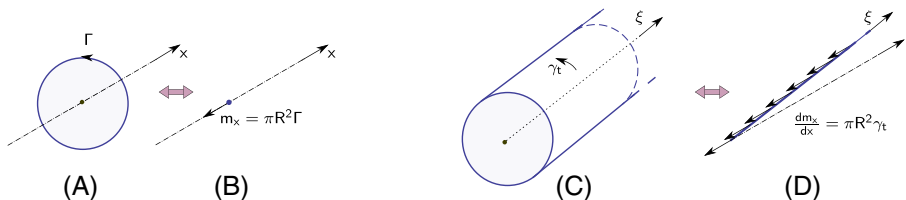


**FIGURE B1** Illustration of the far-field vortex doublet approximation. Vortex ring (A) approximated by a vortex doublet (B). Vortex cylinder (C) approximated by a line doublet (D) [Colour figure can be viewed at [wileyonlinelibrary.com](http://wileyonlinelibrary.com)]

$$u_x(x,r) = -\frac{\gamma_t}{4\pi\sqrt{rR}} \left[ xk(x,r) \left( K(k^2(x,r)) + \frac{R-r}{R+r} \Pi(k^2(0,r), k^2(x,r)) \right) \right]_0^L \quad (C1)$$

$$u_r(x,r) = \frac{\gamma_t}{2\pi} \sqrt{\frac{R}{r}} \left[ \frac{2-k^2(x,r)}{k(x,r)} K(k^2(x,r)) - \frac{2}{k(x,r)} E(k^2(x,r)) \right]_0^L, \quad (C2)$$

where  $k$  is defined in Equation 4 and the term in brackets is the difference between the primitive integral evaluated at  $x = L$  and  $x = 0$ . The integration for the skewed cylinder is also manageable but currently has not been carried out. The far-field formulae for the straight and skewed cylinder are obtained by integrating Equation B1 from  $x_0 = 0$  to  $x_0 = L$ , with  $y_0 = mx_0$ . Equation B2 remains unchanged, but the terms  $I_{*0}$  are given by

$$I_{30} = \left[ \frac{b-c^2x}{(b^2-a^2c^2)(a^2-2bx+c^2x^2)^{1/2}} \right]_0^L, \quad I_{50} = \left[ \frac{b(b^2-3a^2c^2)+2c^2(b^2+a^2c^2)x-6bc^4x^2+2c^6x^3}{(b^2-a^2c^2)^2(a^2-2bx+c^2x^2)^{3/2}} \right]_0^L, \quad (C3)$$

$$I_{51} = \left[ \frac{-a^2(b^2+a^2c^2)+3b(b^2+a^2c^2)x-6b^2c^2x^2+2bc^4x^3}{(b^2-a^2c^2)^2(a^2-2bx+c^2x^2)^{3/2}} \right]_0^L, \quad I_{52} = \left[ \frac{-2a^4b+6a^2b^2x-3b(b^2+a^2c^2)x^2+c^2(b^2+a^2c^2)x^3}{(b^2-a^2c^2)^2(a^2-2bx+c^2x^2)^{3/2}} \right]_0^L. \quad (C4)$$

The expressions given in Equations C3 and C4 are singular for the condition  $b^2 = a^2c^2$ . For this particular case, the following expressions must be used:

$$I_{30} = \left[ \frac{s}{2c(a-scx)^2} \right]_0^L, \quad I_{50} = \left[ \frac{3s}{4c(a-scx)^4} \right]_0^L, \quad I_{51} = \left[ \frac{-a+4scx}{4c^2(a-scx)^4} \right]_0^L, \quad I_{52} = \left[ \frac{s(a^2-4sacx+6c^2x^2)}{4c^3(a-scx)^4} \right]_0^L, \quad (C5)$$

where  $s$  is 1 or  $-1$ , following the sign of  $b$ . The implementation is found in the WIZ package.<sup>28</sup>